

Nanoscale

Accepted Manuscript



This is an *Accepted Manuscript*, which has been through the Royal Society of Chemistry peer review process and has been accepted for publication.

Accepted Manuscripts are published online shortly after acceptance, before technical editing, formatting and proof reading. Using this free service, authors can make their results available to the community, in citable form, before we publish the edited article. We will replace this *Accepted Manuscript* with the edited and formatted *Advance Article* as soon as it is available.

You can find more information about *Accepted Manuscripts* in the [Information for Authors](#).

Please note that technical editing may introduce minor changes to the text and/or graphics, which may alter content. The journal's standard [Terms & Conditions](#) and the [Ethical guidelines](#) still apply. In no event shall the Royal Society of Chemistry be held responsible for any errors or omissions in this *Accepted Manuscript* or any consequences arising from the use of any information it contains.

Enhanced Photoelectrochemical Water Oxidation via Atomic Layer Deposition of TiO₂ on Fluorine-Doped Tin Oxide Nanoparticle Films

Isvar A. Cordova^a, Qing Peng,^a Isa L. Ferrall,^a Adam J. Rieth,^b Paul G. Hoertz,^b Jeffrey T. Glass^a

TiO₂ is an exemplary semiconductor anode material for photoelectrochemical (PEC) water-splitting electrodes due to its functionality, long-term stability in corrosive environments, nontoxicity, and low cost. In this study, TiO₂ photoanodes with enhanced photocurrent density were synthesized by atomic layer deposition (ALD) of TiO₂ onto a porous, transparent, and conductive fluorine-doped tin oxide nanoparticle (nanoFTO) scaffold fabricated by solution processing. The simplicity and disordered nature of the nanoFTO nanostructure combined with the ultrathin conformal ALD TiO₂ coatings offers advantages including decoupling charge carrier diffusion length from optical penetration depth, increased photon absorption probability through scattering, complimentary photon adsorption, and favorable interfaces for charge separation and transfer across the various junctions. In this report, we examine the effects of porosity of the nanoFTO scaffold and thickness of the TiO₂ coating on PEC performance and achieve an optimal photocurrent of 0.7 mA cm⁻² at 0 V vs. Ag/AgCl under 100 mW cm⁻² AM 1.5 G irradiation in a 1 M KOH aqueous electrolyte. Furthermore, the fundamental mechanisms behind the improvements are characterized via cyclic voltammetry, incident photon-to-current efficiency, transient photocurrent spectroscopy, and electrochemical impedance spectroscopy and are contrasted with those of single crystal rutile TiO₂ nanowires. The strategies employed in this work highlight the opportunities inherent to these types of heteronanostructures, where the lessons may be applied to improve the PEC conversion efficiencies of other promising semiconductors, such as hematite (α -Fe₂O₃) and other materials more sensitive to visible light.

1. Introduction

The direct use of sunlight as the electromotive force driving the electrolysis of water is a process known as photoelectrochemical (PEC) water splitting. Given the renewable nature and abundance of solar energy, this PEC process is considered to be the “holy grail” of achieving an economically sustainable and environmentally friendly hydrogen production system.¹ In addition, the storability of hydrogen fuels curbs the intermittency issues intrinsic to the sun’s diurnal cycle. This PEC process is made possible when a semiconductor material² comes into contact with an aqueous electrolyte and causes a depletion region to be created within the semiconductor, forming the semiconductor-liquid junction (SCLJ). The corresponding band bending can drive the separation of photogenerated electrons and holes so that they may undergo the chemical reactions of water oxidation at the anode (oxygen evolution reaction, OER) and water reduction at the cathode (hydrogen evolution reaction, HER), respectively.^{3,4} The HER and OER reactions on the cathode and anode in an alkaline environment are shown in **Equation 1** and **Equation 2**, respectively.



One intrinsically n-type semiconductor material that meets the proper valence and conduction band edge position requirements for the OER is titanium dioxide (TiO₂). Since 1972,⁵ TiO₂ has shown great potential as an exemplary PEC material since it consists of earth-abundant elements, is considered non-toxic, and it is highly stable in a variety of aqueous electrolytes.

Most of the recent approaches to optimizing PEC performance using TiO₂ have deviated from traditional photonic systems with planar morphologies and moved towards employing porous 3-dimensional (3D) nanostructures to enhance the functionality of the PEC devices. The large electrochemically active SCLJ surface area from a 3D porous electrode provides a large contact area between the electrolyte and the electrode, which enables the

usage of a larger portion of the electrode materials to enhance the throughput of the kinetically sluggish OER. Moreover, loading TiO₂ onto a 3D conductive scaffold can decouple the required thickness for efficient light absorption from the minority charge carrier diffusion length and thereby avoid significant recombination of the photogenerated electron/hole pairs. Recent approaches have utilized various conductive 3D nanostructured scaffolds, including Si nanowires⁶, TiSi₂ nanonets⁷, carbon nanotubes,⁸ and even single crystal rutile TiO₂ nanowires⁹ to support TiO₂ for the synthesis of TiO₂ anodes. However, many of these approaches suffer from the fact that the supporting scaffolds are expensive to fabricate and may compete with TiO₂ for the absorption of photons.

To circumvent these problems, our nanostructuring approach utilizes solution-processed transparent conductive oxide (TCO) nanoparticles as a 3D mesoporous scaffold material. The TCO's wide bandgap makes the nanoparticles less likely to compete with the photoactive semiconductor layer. Most recently, Peng *et al.* demonstrated the potential of this approach for the synthesis of TiO₂ PEC electrodes by coating antimony-doped tin oxide nanoparticles (nanoATO) with TiO₂ by atomic layer deposition (ALD).¹⁰ In this study, we demonstrate additional PEC performance enhancements achieved when solution-processed fluorine-doped tin oxide nanoparticles (nanoFTO) are used as the porous TCO scaffold for supporting ALD TiO₂ films. FTO is one of the most commonly used TCOs in optoelectronic applications due to its thermal stability over a wide temperature window and is thus attractive as a mesoporous scaffold. We characterized the TiO₂-coated nanoFTO photoanodes (TiO₂/nanoFTO) by cyclic voltammetry, incident photon-to-current efficiency (IPCE) and transient photocurrent analysis. Importantly, we find that despite the simplicity and disordered nature of the TiO₂/nanoFTO core-shell nanostructure, an extremely effective PEC photoelectrode is created due to the intrinsic benefits of using ultrathin TiO₂ core-shell coatings and specific surface properties inherent to ALD TiO₂. Additional advantages

observed from this particular heterostructure included complimentary photon adsorption from FTO and TiO₂ and a favorable interface for charge separation and transport.

2. Results & Discussion

2.1. Materials Synthesis and Characterization

The self-limiting cyclic layer-by-layer growth mode of ALD enables coating of high aspect ratio nanostructures with angstrom-level thickness precision, conformality, and uniformity. This makes ALD an ideal tool to maximize the performance of the TiO₂/nanoFTO heteronanostructure studied herein. The concept behind using ALD to deposit TiO₂ thin films over the nanoFTO scaffold to construct a PEC photoanode is illustrated in **Figure 1**.

Given that the absorption coefficient of polycrystalline TiO₂ for a 370 nm photon is roughly 1.2 μm,¹¹ a colloidal nanoFTO film with a total thickness of roughly 2 μm was spin-coated onto a planar FTO glass substrate

in order to ensure ample absorption of photons with energies larger than 3.0 eV (bandgap of rutile TiO₂). The resulting nanoFTO scaffold consists of a porous

network of nanoparticles with diameters spanning 100-300 nm. It is expected that the disorder of the nanoFTO scaffold will promote optical scattering effects within the bulk of the film, thus enhancing the light harvesting efficiency of the TiO₂ coatings that serve as the principal photoactive component for PEC water oxidation.

TiO₂ films with thicknesses ranging from 5-20 nm were deposited onto nanoFTO substrates and their resulting chemical composition was characterized by X-ray photoelectron spectroscopy (XPS). **Figure 2** shows XPS spectra of a 10nm TiO₂-coated nanoFTO

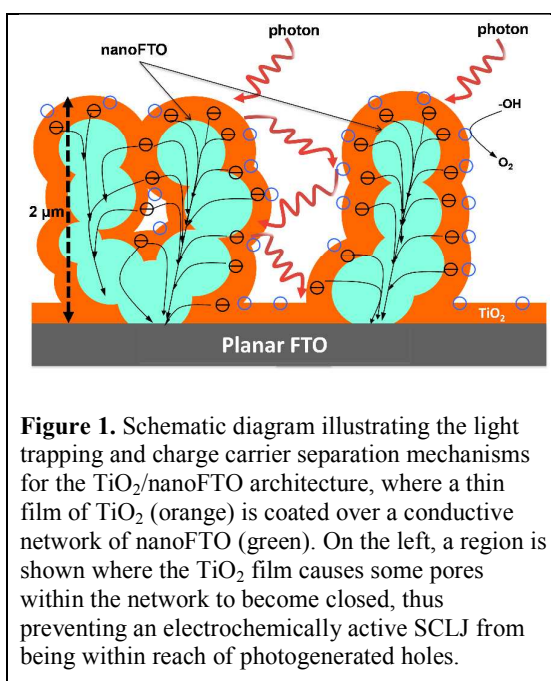
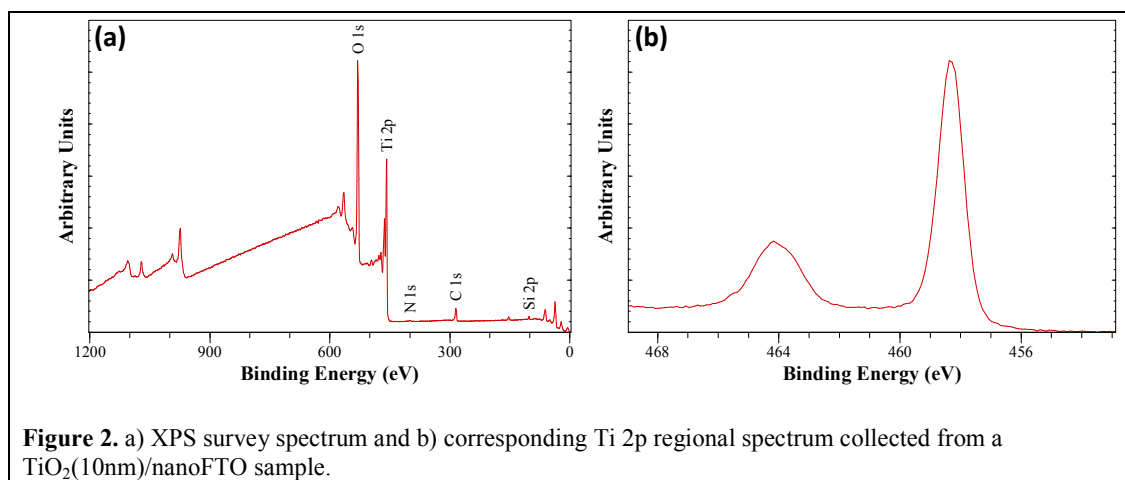


Figure 1. Schematic diagram illustrating the light trapping and charge carrier separation mechanisms for the TiO₂/nanoFTO architecture, where a thin film of TiO₂ (orange) is coated over a conductive network of nanoFTO (green). On the left, a region is shown where the TiO₂ film causes some pores within the network to become closed, thus preventing an electrochemically active SCLJ from being within reach of photogenerated holes.

(TiO₂(10nm)/nanoFTO) sample, which is also representative of the other samples in this study. The survey scan in Figure 2a shows TiO₂ with the presence of N (0.5 at%), C (13.1 at%), and Si (2.2 at%) contaminants. The N and C species can be attributed to the N₂ carrier gas used during ALD^{12, 13} and adventitious carbon, respectively. The presence of small concentrations of Si is likely due to contamination from sample handling and is not expected to contribute to PEC performance. The lack of detection of Sn peaks indicates that a conformal coating of TiO₂ with minimal pinholes was achieved on near the surface of the nanoFTO network. Figure 2b displays the Ti 2p triplet region of the spectrum, whose Ti 2p_{3/2} peak maximum near 538.4 eV confirms the presence of a Ti⁴⁺ oxidation state, which further confirmed the presence of TiO₂.¹⁴ Similar spectra were observed with TiO₂/nanoFTO samples with different TiO₂ coating thicknesses of 5nm-20nm, which suggests that 5nm TiO₂ was able to conformally cover the nanoFTO substrates.



To analyze the crystal structure of TiO₂ ALD coatings onto the nanoFTO structure, Raman spectroscopy was performed on TiO₂/nanoFTO with various thicknesses of TiO₂. **Figure 3** shows the Raman spectra of nanoFTO (cassiterite crystalline phase) and nanoFTO coated with 5, 10, and 20 nm of TiO₂. All the TiO₂/nanoFTO samples show strong Raman modes near 242 cm⁻¹, 440 cm⁻¹, and 610 cm⁻¹, which are the three strongest Raman bands associated with the rutile polymorph of TiO₂.¹⁵ As anatase TiO₂ is the usual polymorph at this

low growth temperature,¹⁶ we attribute this preferential rutile formation to the underlying cassiterite lattice structure of the nanoFTO, which is from the rutile family and possesses similar lattice constants as rutile TiO₂. This is consistent with recent studies that show

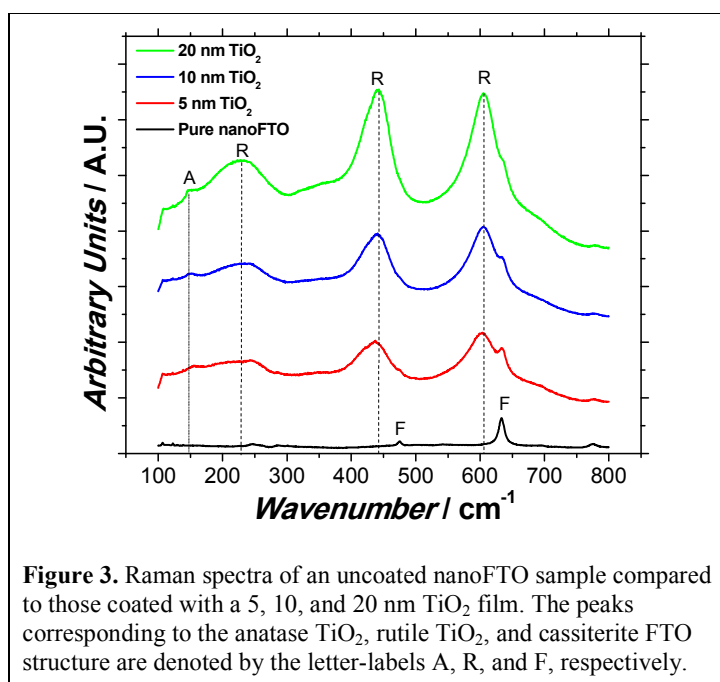
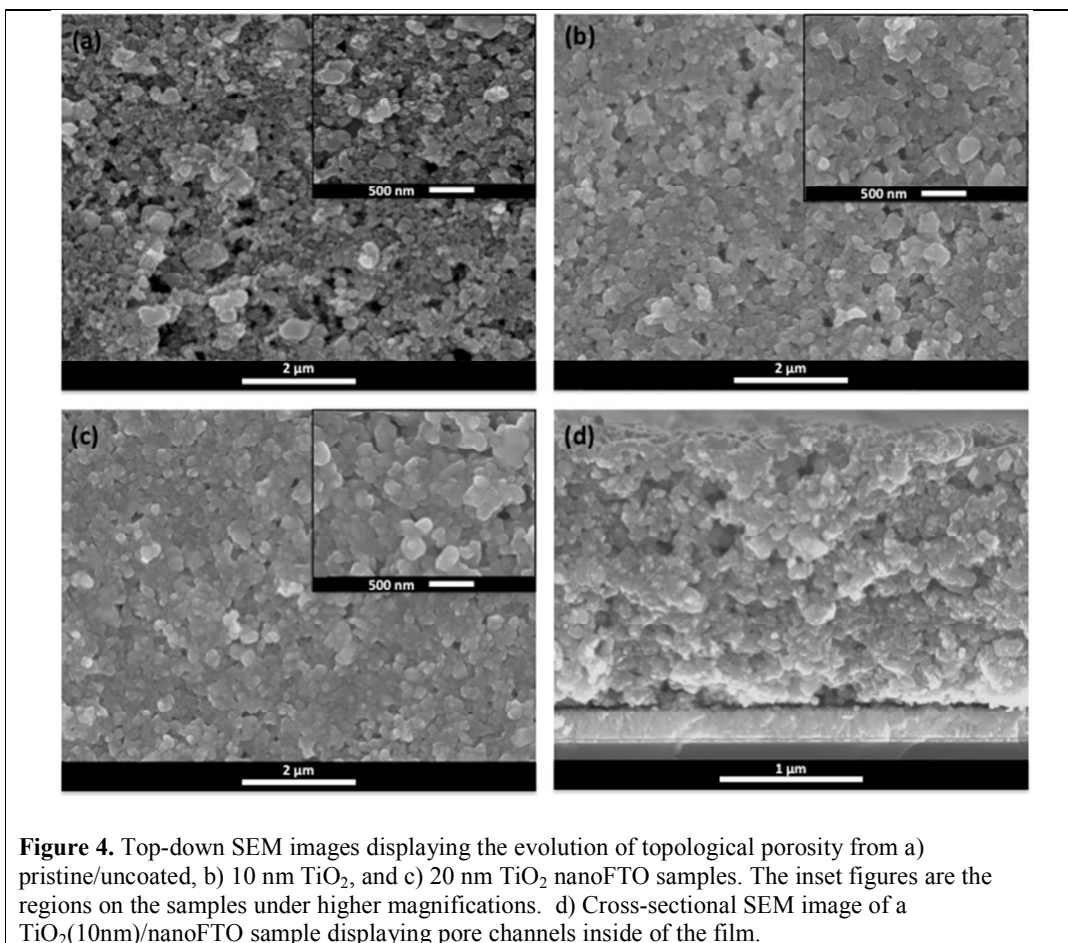


Figure 3. Raman spectra of an uncoated nanoFTO sample compared to those coated with a 5, 10, and 20 nm TiO₂ film. The peaks corresponding to the anatase TiO₂, rutile TiO₂, and cassiterite FTO structure are denoted by the letter-labels A, R, and F, respectively.

a preferential formation of rutile TiO₂ via ALD when deposited on rutile-like substrates at low growth temperatures.^{10, 17, 18} Interestingly, as the film thickness increases, a small peak corresponding to the major anatase TiO₂ Raman band near 143 cm⁻¹ starts to be detected, as shown by the TiO₂(20nm)/nanoFTO sample. This suggests that although our polycrystalline TiO₂ material consists mostly of the rutile phase, some TiO₂ crystals with the anatase phase might also be present in small concentrations.

Figure 4 contains scanning electron micrographs (SEMs) of TiO₂/nanoFTO samples as the TiO₂ coating thickness is increased. The plain-view SEMs in Figures 4a-c show the transition from the wide distribution of open pores (dark regions) provided by the uncoated nanoFTO scaffold (Figure 4a) to the sample with the thickest TiO₂ film (Figure 4c), where the density of visible pores has been drastically reduced. In contrast, the TiO₂(10nm)/nanoFTO sample displayed in Figure 4b shows an intermediate state where the smallest pores may have been filled but the larger pores remain. The cross-sectional perspective in Figure 4d, shows the larger pore channels through which the TiO₂(10nm)/nanoFTO photoelectrode maintained electrolyte accessibility throughout the depth of the nanostructure.

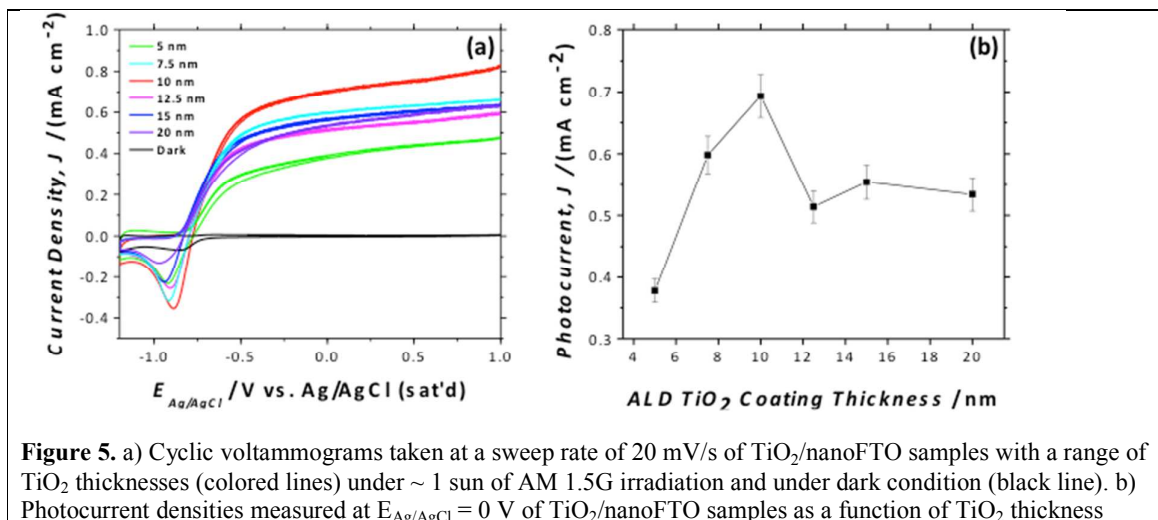


2.2. Photoelectrochemical Performance

2.2.1. Photocurrent Optimization

Figure 5 displays the photocurrent density (J) as a function of the applied potential versus an Ag/AgCl (KCl sat[']) reference electrode ($E_{\text{Ag}/\text{AgCl}}$) and was obtained by performing linear cyclic voltammetry scans on TiO₂/nanoFTO photoelectrodes with a range of TiO₂ thickness. The consistent diode-like shape (or fill factor) across all of the photocurrent responses plotted in Figure 5a confirms the conformal coverage of the ALD TiO₂ coating over the entire surface area of the underlying nanoFTO. In addition, the cathodic peak observed at $E_{\text{Ag}/\text{AgCl}} = -0.9$ V corresponds to the oxygen reduction reaction resulting from ineffective purging of the recently evolved O₂ within the mesoporous nanostructure. Figure 5a shows that the TiO₂(10 nm)/nanoFTO produces a photocurrent density of 0.7 mA/cm² at $E_{\text{Ag}/\text{AgCl}} = -0$ V. This is the maximum J observed among various TiO₂ film thicknesses and can henceforth be

considered to be the optimal thickness for this particular nanostructure. This value represents an almost fourfold enhancement over the recently reported values for planar ALD TiO₂/FTO and is even higher than the 0.58 mA/cm² photocurrent density value which was recently observed with nanoATO.¹⁰ Figure 5b summarizes the $J-E_{Ag/AgCl}$ data in order to help to visualize the effect of thickness on photocurrent. At thicknesses less than 10 nm, there is a high surface area in contact with the electrolyte, allowing a large concentration of reactive sites to be available for the OER. However, there is not enough TiO₂ to absorb and convert an optimal number of photons, which is evidenced by the Incident Photon-to-Current Efficiency (IPCE) measurements presented in the following section. As the thickness increases to 10 nm, the smaller pores may begin to be filled (as shown in the SEM from Figure 4). However, any detrimental effects on PEC performance caused by a decrease in active surface area are likely outweighed by a boost in light absorption from the higher loading density of the photoactive TiO₂ coating (**Figure S3**). As the thickness of TiO₂ coatings becomes larger than 10 nm, the majority of the pores become filled which causes a sharp drop in photocurrent. The filling of larger pores reduces the active surface area and increases the hole transport lengths, counteracting the benefit of adding photoactive TiO₂. These competing contributions account for the leveling off of J . Thereafter, J is expected to continue to decrease as the last pores become filled in a manner similar to a previous study.¹⁰ As for the stability of these samples, within the roughly 30 minute time period required for most experiments, no obvious degradation of the photocurrent is observed for any of the TiO₂/nanoFTO samples. Even more, the $J-E_{Ag/AgCl}$ curves from a TiO₂(10nm)/nanoFTO sample that had been stored in air and then retested periodically in 1 M KOH over the course of approximately 1 year displayed no significant signs of degradation (**Figure S4**).



2.2.2. Incident Photon-to-Current Efficiency (IPCE)

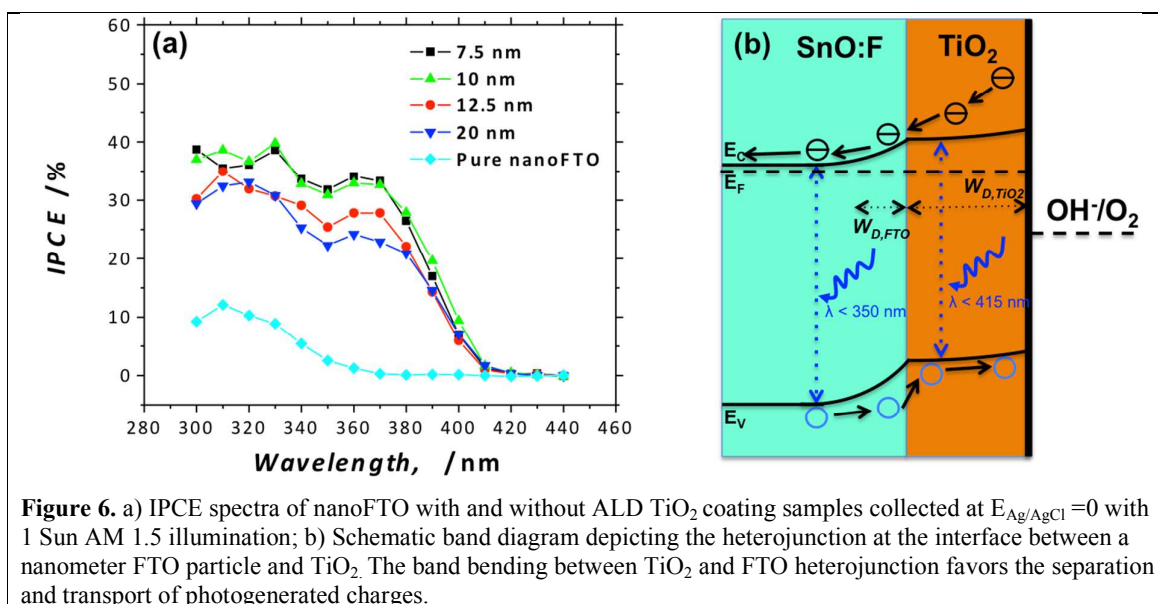
IPCE measurements were conducted on the photoelectrodes to gain additional insight into the wavelength-dependent photon absorbance, carrier separation, charge transport, and interfacial charge transfer mechanisms related to the total photocurrents observed above. IPCE spectra of various samples and a schematic of the corresponding mechanisms are shown in **Figure 6**. The IPCE spectra displayed in Figure 6a were collected at E_{Ag/AgCl}=0, thus characterizing the mechanisms behind the photocurrents observed in Figure 5b. As expected from the data above, the TiO₂(10nm)/nanoFTO IPCE curve shows the highest overall efficiencies. The IPCE curve of TiO₂(7.5nm)/nanoFTO closely matched the IPCE behavior of the TiO₂(10nm)/nanoFTO sample at wavelengths (λ) less than 380 nm, but its values are smaller at wavelengths longer than 380 nm. The smaller IPCE at these longer wavelengths accounts for the lower total photocurrent performance of TiO₂(7.5nm)/nanoFTO in comparison with TiO₂(10nm)/nanoFTO (Figure 5a), despite the fact that the overall area under each IPCE curve is similar for both samples. This is because of a much higher weighting factor for photons near 400 nm in the simulated solar spectrum (AM 1.5 G) than the photons with shorter wavelengths deeper into the UV region.¹⁹

It is also important to note the relatively high IPCE efficiencies obtained for the higher energy UV photons (below 350 nm wavelengths) in all the TiO₂/nanoFTO electrodes. For

other reported TiO₂-based nanostructured photoelectrodes, the IPCE values peak and then decrease dramatically as the wavelengths decrease.^{17,20} As an example, we confirmed this behavior for 1.8 μm TiO₂ nanowires (NWs) on planar FTO glass, which show IPCE values that peak around 380 nm and decrease sharply at shorter wavelengths (**Figure S1**). This is due to a larger recombination ratio for photoelectrons excited by shorter wavelength, which tend to be generated near the tips of the nanowires and thus have a high probability of recombining as they are transported throughout the micrometer-long NWs. However, such behavior is not the case here for the TiO₂-coated nanoFTO electrodes; the high IPCE values are sustained down to a wavelength of 300 nm. We attribute this efficient behavior to the unique ALD TiO₂/nanoFTO hetero-nanostructure.

The underlying nanoFTO support plays several roles here. First, the high electron conductivity of the FTO nanoparticles decreases the transport time needed for electrons to reach the collecting electrode. When this is combined with the short distance that holes photogenerated within the thin TiO₂ coating need to travel before reaching the SCLJ, the high electron conductivity decreases the recombination rate of the electron-hole pairs. This is especially important for the electron-hole pairs that are generated from high-energy photons, since they will be absorbed near the top surface of the electrode due to their large absorption cross-section.^{17,20} Second, nanoFTO will transmit or scatter photons with energy smaller than 3.5 eV. Although this means that it will not compete with TiO₂ for the absorption of photons with energies between 3.0-3.5 eV, the absorbance of such photons within thin TiO₂ coatings (≤ 20 nm) is normally very small. However, due to the 3D morphology of the nanoFTO scaffold, the probability that the TiO₂ coating will absorb these photons will be dramatically increased as they scatter and propagate through the tortuous pathway inside the TiO₂-coated FTO nanoparticles. Third, the IPCE spectrum of nanoFTO without ALD coating indicates that the nanoFTO support will absorb photons with energies greater than 3.5 eV ($\lambda < 350$ nm) and convert them into useful electron-hole pairs. Based on the respective positions of the

conduction and valence band edges of FTO and TiO₂, a type II heterojunction is formed between FTO and TiO₂ that promotes charge transport across the semiconductor junction in the desired directions for the OER.²¹ The approximately 40% IPCE values imply that the nanoFTO is not only absorbing a large number of the incident photons with $\lambda < 350$ nm, but is also helping to separate the photogenerated carriers efficiently at the heterojunction with TiO₂. We postulate that an additional reason for this rapid charge separation may be due to the reported intermixing of the electronic structure of FTO and TiO₂ near the heterojunction, which may cause a small potential distribution to be felt near this interface.²² In addition, it is possible that the complete depletion of the ultrathin TiO₂ coating at $E_{Ag/AgCl} = 0$ may cause the total width of any depletion layer ($W_{D,Total} = W_{D,FTO} + W_{D,TiO_2}$) to extend a small distance into the nanoFTO structure. The strength of the electric field (amount of band bending) within TiO₂ is expected to be small due to the ultrathin dimensions of the ALD TiO₂ coatings.²³ Although there have been reports of small scale band bending inducing the photooxidation of water on TiO₂,²⁴ we ascribe most of the charge separation within our ALD TiO₂ films to their long diffusion lengths (10-100 nm)²⁵⁻²⁷ by which they will reach the SCLJ and become rapidly scavenged by the OH⁻/O₂ redox-driven free energy gradient on the surface.²⁸ On the other hand, within the nanoFTO, the formation of the depletion layer might provide the electric field required to efficiently separate the photogenerated charges (Figure 6b). This kind of extension of the depletion layer into the underlying TCO material has been reported for anatase TiO₂ thin films on tin-doped indium oxide.²⁹ In summary, the combined effects of these above-mentioned mechanisms help to produce the unique IPCE behavior of these ALD TiO₂/nanoFTO nanostructured photoanodes.



2.2.3. Characterization of Recombination Mechanisms

To help further understand the charge transfer mechanisms of the TiO₂/nanoFTO samples, we analyzed their transient photocurrent behavior from chopped illumination and contrasted it with the performance of a sample of hydrothermally-grown rutile TiO₂NW/FTO with similar photocurrents (**Figure 7**). The measurement of these non-steady state photocurrents can be used to study recombination mechanisms since the characteristic relaxation time for minority carriers trapped in surface states or accumulated near the surface is slow enough to be detected experimentally.³⁰

Figure 7a shows the similar levels of total photocurrent performance for both of these samples under chopped illumination as well as a saturation of photocurrent transient effects as a function of additional negative bias. Since the photocurrent transient effects are more pronounced near the onset of photocurrent, we chose to compare their transient behavior during an amperometric scan conducted at a constant potential of $E_{Ag/AgCl} = -0.8V$. This low band-bending region is expected to highlight the recombination due to the accumulation of holes and surface states, and not be subject to the effect of photon flux.³¹ The symmetry of the anodic and cathodic transients observed for each sample indicated that both samples suffered

from these recombination mechanisms. However, the drastically larger transient peak current feature observed from the TiO₂ NW sample indicates a loss of a significantly higher fraction of photogenerated charges³² than the ALD TiO₂/nanoFTO sample. The dramatic difference in charge transfer mechanisms between TiO₂/nanoFTO and rutile NWs is also highlighted by their different impedance response under EIS, whose Nyquist plot shows an additional charge transfer (semicircular) feature at low frequencies only for the rutile NWs (**Figure S2**). This indicates that the surface of the ALD TiO₂ allows more facile charge transfer across the SCLJ.^{33, 34}

In highly alkaline 1 M KOH, two possibilities have been previously proposed as explanations for the faster surface hydroxide-driven reaction kinetics³⁵ observed on certain rutile TiO₂ materials. The two possibilities are i) the presence of multiple rutile crystal facets, and ii) a higher concentration of oxygen vacancies on the film's surface.³⁶ Both of these are possible given the polycrystalline and defective growth mechanism inherent to ALD. However, a more intriguing possibility is the generation of more peroxide (H₂O₂) species generated only near the surface³¹ which serve as hole scavengers³⁷ and thus accelerate the OER.³² Given the slightly more negative redox potential for OH⁻/H₂O₂ than OER,²¹ such peroxides could be generated more easily if "hot holes" reached the surface before having time to relax down to the valence band edge by thermalization. However, assuming that the thermalization time is just under 100 ps for n-TiO₂³⁸ and that the hole transit time through a full depletion layer is less than 40 ps,²¹ it may be possible that the efficient collection and utilization of the deep UV photons by the TiO₂/nanoFTO photoelectrodes could be yielding such behavior. This may be even more likely for the nanoFTO system, given the ultrathin nature of the ALD TiO₂ films that would result in even shorter theoretical hole transit times. Although the feasibility of such behavior is still under some debate, there have been some reports claiming that it can be sustained across the SCLJ using oxide-covered metallic electrodes.^{39, 40}

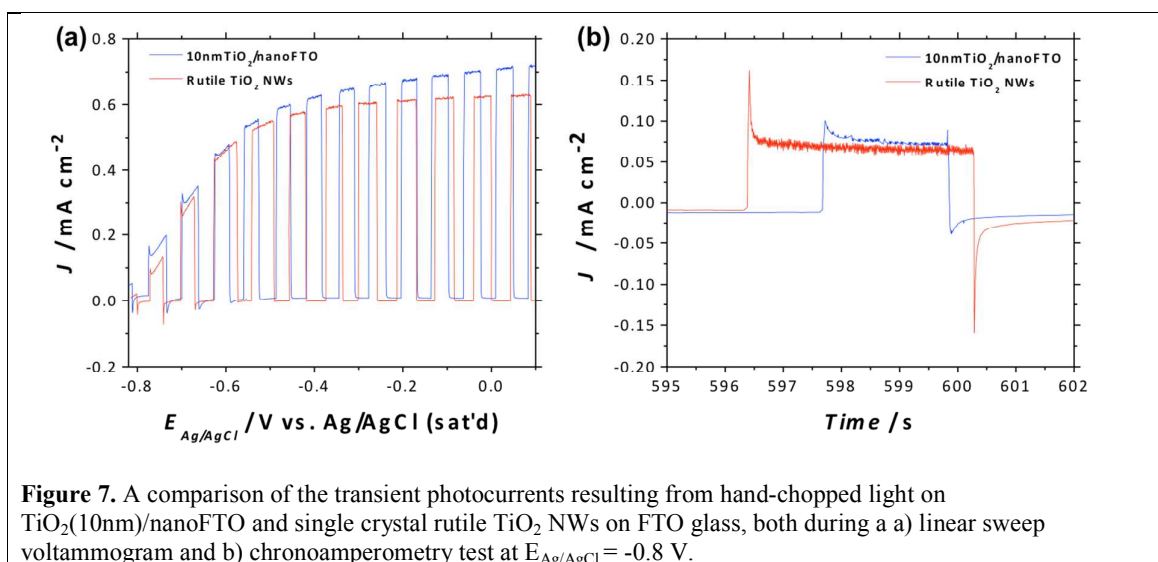


Figure 7. A comparison of the transient photocurrents resulting from hand-chopped light on TiO₂(10nm)/nanoFTO and single crystal rutile TiO₂ NWs on FTO glass, both during a a) linear sweep voltammogram and b) chronoamperometry test at $E_{Ag/AgCl} = -0.8$ V.

3. Conclusion

We have shown that the ALD TiO₂/nanoFTO nanostructure resulted in a photoanode with impressive light harvesting efficiency for the photooxidation of water. In particular, the high IPCE efficiencies of TiO₂/nanoFTO throughout their materials' respective absorption regions provide insights for future development of tandem heteronanostructures for applications in PEC conversion and solar cells. Moreover, the photocurrent transient behavior indicates charge transfer mechanisms on the surface of these nanostructures is extremely efficient and could be a property inherent to these ultrathin ALD films. Given the large junction area that is responsible for the photocurrent enhancement, future work should be done to characterize the specific electronic properties and chemical bonding structure near the interface between the ALD TiO₂ and the nanoFTO, as it is possible that the *d* orbital occupancy has been modified near this transition metal oxide interface.²² We expect that future applications could exploit the beneficial effects observed herein to further improve the PEC conversion efficiencies of other promising materials such as hematite (α -Fe₂O₃).

4. Experimental Methods

Synthesis of nanoFTO-coated Substrates

FTO nanopowder (3 g, Keeling and Walker, 0.1 - 0.3 microns, BET surface area 10-15 m²) was added to 200 proof ethanol (10 mL) to make a suspension of nanoFTO as discussed previously.⁴¹ The application of nanoFTO onto 12 mm x 50 mm FTO-coated Soda lime glass (Hartford Glass, 15 ohm/sq) was accomplished by spin-coating the nanoFTO suspension according to earlier procedures.^{10, 42} Finally, the approximately 2 μm thick layer of nanoFTO was sintered at 450 °C for 2 hours before the ALD process.

Atomic Layer Deposition (ALD)

The TiO₂ films were deposited on the nanoFTO-coated substrates described above by a “homemade” hot-wall viscous flow ALD reactor operated at 300 °C. The reactor was kept at process pressure of 1.42 Torr under a constant 300 sccm flow of UHP nitrogen (Airgas Inc.) as a carrier and purging gas. TiCl₄ and deionized H₂O were used as the metal precursor and the co-reactant, respectively, for the TiO₂ ALD process. All precursors were held at the temperature of ~ 40 °C. The time sequence of the recipe used was 1.5/5 and 1.5/5 s for the TiCl₄ dose/purge and H₂O dose/purge, respectively. Prior to growth, substrates were blown dry with UHP nitrogen before loading them into the ALD chamber. During each growth run, p-type Si (100) substrates covered with a native oxide layer were placed along the length of the reactor as the control samples to monitor the film thickness. Film thickness was measured by using a J.A. Woollam M-88 Variable Angle Spectroscopic Ellipsometer at scan angles ranging from 65-75° and a polarizer angle of 20°. These thicknesses corresponded to the thickness of the films deposited on the nanoFTO glass substrates since the growth rate has been shown to be the same on Si as on FTO (⁴³). 5, 7.5, 10, 12.5, 15, and 20 nm TiO₂ films were deposited using 120, 171, 225, 270, 318, and 410 ALD cycles, respectively. The measured growth rate was approximately 0.5 Å per cycle.

Material Characterization

The chemical compositions of TiO₂ films were characterized by X-ray photoelectron spectroscopy (XPS) using a Kratos Analytical Axis Ultra equipped with a monochromated Al K- α x-ray source operated at an emission current of 10 mA with an accelerating voltage of 15 kV. Pass energies of 20 eV and 160 eV were used for regional and survey scans, respectively. The step sizes were 0.1 eV and 1 eV for the regional and survey scans, respectively. All XPS spectra were processed with CasaXPS software, and were calibrated to an adventitious carbon peak near 284.6 eV. The crystallinity of the films was characterized by Raman spectroscopy via an Horiba Jobin Yvon LabRam ARAMIS Raman microscope with a 633 nm He/Ne laser. The morphologies of samples were imaged using an FEI XL30 Scanning Electron Microscope (SEM) under a high-resolution mode with electron beam energy of 15 kV. Lastly, optical measurements from the TiO₂/nanoFTO nanostructure was collected at UNC-Chapel Hill using a Cary 5000 UV-Vis spectrometer with the DRA-2500 internal integrating sphere accessory. Using a planar FTO sample as the blank for reference, reflectance and transmittance data were measured in order to calculate the amount of absorption plus scattering (that couldn't be accounted for by the integrated sphere) taking place in our samples according to the formula $100 - T - R = A + S$, where T is the total transmittance, R is the total reflectance, A is the absorption, and S is the unaccounted scattered light.

PEC Performance Characterization

All electrical connections were made by scratching the ALD film to expose part of the underlying FTO surface. The scratched region was then rubbed with InGa eutectic metal (Sigma-Aldrich, 495425) in order to ensure an ohmic contact with low resistance between the FTO coating on the glass and the flattened end of a bare Cu wire used as the electrode lead. This contact region was then sealed with a nonconductive epoxy (Hysol 9460, Loctite) and left to cure for at least two hours. In order to isolate all non-semiconductor (inactive)

components from the electrolyte, the rest of the length copper wire was fed through a quartz glass tube (Ace Glass, O.D. 6mm) and the active planar PEC area was defined by covering all inactive regions of each sample with the same nonconductive epoxy resin. Electrochemical activity was measured using a Bio-Logic SP-200 potentiostat. An Oriel 150 W Xe Arc lamp with an AM 1.5 G filter was used as the light source with the calibrated power of 100 mWcm^{-2} on the sample surface. All measurements were performed with a 1 M KOH electrolyte and under a constant flow of Ar as the sparging gas, via a standard three-electrode configuration with a Pt mesh as the counter electrode and an Ag/AgCl (saturated in KCl) reference electrode (0.198 V vs. standard hydrogen electrode). To measure the basic photoresponse, cyclic voltammetry (CV) scans were taken at a voltage sweep rate of 20 mV/s. The photocurrent density was then obtained by dividing the photocurrent by the photoactive area of the electrode, which was measured through scale-marked photos via Image-J. The electrochemical impedance spectroscopy (EIS) measurements were performed under both dark and light conditions. The amplitude of the sinusoidal voltage was 10 mV and it was applied across a frequency range from 1 MHz to 1 mHz. Mott-Schottky analyses were derived from the EIS measurements at the frequency of 1 kHz. The incident photon-to-current efficiency (IPCE) data was collected at 0 V vs. Ag/AgCl using a customized Newport-Oriel system powered by a 300 W Xe (Ozone-free) lamp equipped with a Cornerstone 130 1/8 M Monochromator. The irradiance was measured with a power meter (Newport 1918-R) adjusted to the calibrated photoresponse of a standard silicon photodetector.

Rutile TiO₂ Nanowire Synthesis

The hydrothermal synthesis procedure of TiO₂ nanowires on a FTO glass substrate is similar as the literature report. The reaction solution was made by mixing 5 ml concentrated HCl (ACS, ~37%,) with 5 ml de-ionized (DI) water, followed by addition of 0.16 ml of titanium butoxide (Reagent Grade, Sigma Aldrich). The solution was stirred for 10 min before

transferred into a hydrothermal autoclave reactor, which has a volume of 20 ml. A cleaned FTO glass substrate, which was sonicated in soap water, DI water, ethanol, and DI water sequentially, was then leaned against the wall of the Teflon lined autoclave with the FTO coated surface facing downwards. The sealed autoclave was then transferred into a furnace and sit in the furnace for 2h at 200 °C. After the reaction, DI water was used to cool down the autoclave to room temperature before open it. Then the FTO substrate coated with uniform pale white film of TiO₂ nanowire (NW) was recovered and rinsed thoroughly by DI water, and dried in air. The synthesized TiO₂NW/FTO samples were then annealed in air at 500 °C for 2h before assembled into a testable electrode.

Acknowledgements

This work was performed with financial support from RTI International, Research Triangle Solar Fuels Institute, and UNC Energy Frontier Research Center (EFRC) “Center for Solar Fuels;” under US DOE Office of Basic Energy Science award DE-SC0001011 and UNC “Solar Energy Research Center Instrumentation Facility” (SERC) funded by the U.S. Department of Energy Office of Energy Efficiency & Renewable Energy under award number DE-EE0003188. The authors would like to acknowledge the assistance of Dr. Charles B. Parker, James B. Thostenson, Shane T. DiDona, Matthew K. Brennaman, and the staff of the Duke Shared Materials Instrumentation Facility throughout this study.

Notes and References:

^a Electrical and Computer Engineering Department

Duke University, Durham, NC, 27708, USA.

Email: isvar.cordova@duke.edu; qing.peng@duke.edu; jeff.glass@duke.edu

^b RTI International, Durham, NC, 27709, USA.

1. Y. Tachibana, L. Vayssieres and J. R. Durrant, *Nat. Photonics*, 2012, 6, 511-518.
2. M. G. Walter, E. L. Warren, J. R. McKone, S. W. Boettcher, Q. Mi, E. A. Santori and N. S. Lewis, *Chemical Reviews*, 2010, 110, 6446-6473.
3. M. Gratzel, *Nature*, 2001, 414, 338-344.
4. M. S. Prévot and K. Sivula, *The Journal of Physical Chemistry C*, 2013, 117, 17879-17893.
5. A. Fujishima and K. Honda, *Nature*, 1972, 238, 37-+.
6. Y. J. Hwang, A. Boukai and P. D. Yang, *Nano Letters*, 2009, 9, 410-415.
7. Y. J. Lin, S. Zhou, X. H. Liu, S. Sheehan and D. W. Wang, *J. Am. Chem. Soc.*, 2009, 131, 2772-+.
8. C. L. Pint, K. Takei, R. Kapadia, M. Zheng, A. C. Ford, J. J. Zhang, A. Jamshidi, R. Bardhan, J. J. Urban, M. Wu, J. W. Ager, M. M. Oye and A. Javey, *Advanced Energy Materials*, 2011, 1, 1040-1045.
9. Y. J. Hwang, C. Hahn, B. Liu and P. Yang, *Acs Nano*, 2012, 6, 5060-5069.
10. Q. Peng, B. Kalanyan, P. G. Hoertz, A. Miller, D. H. Kim, K. Hanson, L. Alibabaei, J. Liu, T. J. Meyer, G. N. Parsons and J. T. Glass, *Nano Letters*, 2013, 13, 1481-1488.
11. A. Linsebigler, G. Q. Lu and J. T. Yates, *J Chem Phys*, 1995, 103, 9438-9443.
12. M. L. Kaariainen and D. C. Cameron, *Thin Solid Films*, 2012, 526, 212-217.
13. H. E. Cheng, W. J. Lee, C. M. Hsu, M. H. Hon and C. L. Huang, *Electrochem Solid St*, 2008, 11, D81-D84.
14. M. C. Biesinger, L. W. M. Lau, A. R. Gerson and R. S. C. Smart, *Applied Surface Science*, 2010, 257, 887-898.
15. S. W. Lu, C. Harris, S. Walck and M. Arbab, *J Mater Sci*, 2009, 44, 541-544.
16. M. Ritala, M. Leskela, E. Nykanen, P. Soinenen and L. Niinisto, *Thin Solid Films*, 1993, 225, 288-295.
17. Y. J. Hwang, C. Hahn, B. Liu and P. D. Yang, *Acs Nano*, 2012, 6, 5060-5069.
18. H. E. Cheng, C. M. Hsu and Y. C. Chen, *J Electrochem Soc*, 2009, 156, D275-D278.
19. Z. Chen, H. N. Dinh and E. Miller, Springer New York, S.I., 2013, p. 1 online resource.
20. I. S. Cho, M. Logar, C. H. Lee, L. L. Cai, F. B. Prinz and X. L. Zheng, *Nano Letters*, 2014, 14, 24-31.
21. R. v. d. Krol and M. Grätzel, in *Electronic Materials: Science & Technology*, Springer, New York, 2012, pp. 1 online resource (viii, 321 pages).
22. C. X. Kronawitter, M. Kapilashrami, J. R. Bakke, S. F. Bent, C. H. Chuang, W. F. Pong, J. H. Guo, L. Vayssieres and S. S. Mao, *Physical Review B*, 2012, 85.
23. A. J. Bard and M. Stratmann, *Encyclopedia of electrochemistry*, Wiley-VCH, Weinheim, 2001.
24. Z. Zhang and J. T. Yates, *Chemical Reviews*, 2012, 112, 5520-5551.
25. S. Hoang, S. W. Guo, N. T. Hahn, A. J. Bard and C. B. Mullins, *Nano Letters*, 2012, 12, 26-32.
26. A. L. Linsebigler, G. Q. Lu and J. T. Yates, *Chemical Reviews*, 1995, 95, 735-758.
27. P. Salvador, *J. Appl. Phys.*, 1984, 55, 2977-2985.

28. L. M. Peter and D. Vanmaekelbergh, in *Advances in Electrochemical Science and Engineering*, Wiley-VCH Verlag GmbH, 2008, DOI: 10.1002/9783527616800.ch2, pp. 77-163.
29. R. vandeKrol, A. Goossens and J. Schoonman, *J Electrochem Soc*, 1997, 144, 1723-1727.
30. J. Li and L. M. Peter, *J Electroanal Chem*, 1985, 193, 27-47.
31. D. Tafalla, P. Salvador and R. M. Benito, *J Electrochem Soc*, 1990, 137, 1810-1815.
32. P. Salvador, *J. Phys. Chem.*, 1985, 89, 3863-3869.
33. L. Bertoluzzi and J. Bisquert, *J Phys Chem Lett*, 2012, 3, 2517-2522.
34. B. Klahr, S. Gimenez, F. Fabregat-Santiago, J. Bisquert and T. W. Hamann, *J. Am. Chem. Soc.*, 2012, 134, 16693-16700.
35. A. Imanishi, T. Okamura, N. Ohashi, R. Nakamura and Y. Nakato, *J. Am. Chem. Soc.*, 2007, 129, 11569-11578.
36. T. Kisumi, A. Tsujiko, K. Murakoshi and Y. Nakato, *J Electroanal Chem*, 2003, 545, 99-107.
37. H. Dotan, K. Sivula, M. Gratzel, A. Rothschild and S. C. Warren, *Energy & Environmental Science*, 2011, 4, 958-964.
38. N. S. Lewis, *Annual Review of Physical Chemistry*, 1991, 42, 543-580.
39. Y. E. Sung and A. J. Bard, *J Phys Chem B*, 1998, 102, 9806-9811.
40. A. J. Nozik and R. Memming, *J. Phys. Chem.*, 1996, 100, 13061-13078.
41. C. A. Kent, J. J. Concepcion, C. J. Dares, D. A. Torelli, A. J. Rieth, A. S. Miller, P. G. Hoertz and T. J. Meyer, *J. Am. Chem. Soc.*, 2013, 135, 8432-8435.
42. P. G. Hoertz, Z. F. Chen, C. A. Kent and T. J. Meyer, *Inorg Chem*, 2010, 49, 8179-8181.
43. D. H. Kim, Ph.D. Doctor of Philosophy, North Carolina State University, 2013.